

## Electromagnetic and thermal properties of three-dimensional printed multilayered nano-carbon/poly(lactic) acid structures

A. Paddubskaya, N. Valynets, P. Kuzhir, K. Batrakov, S. Maksimenko, R. Kotsilkova, H. Velichkova, I. Petrova, I. Biró, K. Kertész, G. I. Márk, Z. E. Horváth, and L. P. Biró

Citation: *Journal of Applied Physics* **119**, 135102 (2016); doi: 10.1063/1.4945576

View online: <http://dx.doi.org/10.1063/1.4945576>

View Table of Contents: <http://scitation.aip.org/content/aip/journal/jap/119/13?ver=pdfcov>

Published by the [AIP Publishing](#)

---

### Articles you may be interested in

[Microstructure, elastic and electromagnetic properties of epoxy-graphite composites](#)

*AIP Advances* **5**, 067137 (2015); 10.1063/1.4922872

[Thermal property and assessment of biocompatibility of poly\(lactic-co-glycolic\) acid/graphene nanocomposites](#)

*J. Appl. Phys.* **115**, 054701 (2014); 10.1063/1.4864263

[Epoxy composites filled with high surface area-carbon fillers: Optimization of electromagnetic shielding, electrical, mechanical, and thermal properties](#)

*J. Appl. Phys.* **114**, 164304 (2013); 10.1063/1.4826529

[Electromagnetic absorption and shielding behavior of polyaniline-antimony oxide composites](#)

*AIP Conf. Proc.* **1512**, 1218 (2013); 10.1063/1.4791489

[High frequency electromagnetic interference shielding response of mixtures and multilayer films based on conducting polymers](#)

*J. Appl. Phys.* **88**, 513 (2000); 10.1063/1.373688

---



**NEW Special Topic Sections**

**NOW ONLINE**  
Lithium Niobate Properties and Applications:  
Reviews of Emerging Trends

**AIP** | Applied Physics Reviews

# Electromagnetic and thermal properties of three-dimensional printed multilayered nano-carbon/poly(lactic) acid structures

A. Paddubskaya,<sup>1,2</sup> N. Valynets,<sup>1</sup> P. Kuzhir,<sup>1,3,a)</sup> K. Batrakov,<sup>1</sup> S. Maksimenko,<sup>1,3</sup>  
 R. Kotsilkova,<sup>4</sup> H. Velichkova,<sup>4</sup> I. Petrova,<sup>4</sup> I. Biró,<sup>5,b)</sup> K. Kertész,<sup>6,c)</sup> G. I. Márk,<sup>6,c)</sup>  
 Z. E. Horváth,<sup>6,c)</sup> and L. P. Biró<sup>6,c)</sup>

<sup>1</sup>Research Institute for Nuclear Problems, Belarusian State University, Bobruiskaya Str. 11, 220030 Minsk, Belarus

<sup>2</sup>Center for Physical Sciences and Technology, A. Goštauto 11, LT-01108 Vilnius, Lithuania

<sup>3</sup>Tomsk State University, Tomsk 634050, Russian Federation

<sup>4</sup>Open Laboratory on Experimental Micro and Nano Mechanics, Institute of Mechanics, Bulgarian Academy of Sciences, Acad. G. Bonchev Str., Block 4, Sofia, Bulgaria

<sup>5</sup>3D Wishes, Bíró u. 44/a/2, Erd, Hungary

<sup>6</sup>Institute of Technical Physics and Materials Science, Centre for Energy Research, PO Box 49, 1525 Budapest, Hungary

(Received 20 January 2016; accepted 24 March 2016; published online 7 April 2016)

A new type of light-weight material produced by 3D printing consisting of nano-carbon doped polymer layer followed by a dielectric polymer layer is proposed. We performed temperature dependent characterization and measured the electromagnetic (EM) response of the samples in the GHz and THz range. The temperature dependent structural characteristics, crystallization, and melting were observed to be strongly affected by the presence and the number of nano-carbon doped layers in the sandwich structure. The electromagnetic measurements show a great potential of such a type of periodic material for electromagnetic compatibility applications in microwave frequency range. Sandwich structures containing only two nano-carbon layers already become not transparent to the microwaves, giving an electromagnetic interference shielding efficiency at the level of 8–15 dB. A sandwich consisting of one nano-carbon doped and one polymer layer is opaque for THz radiation, because of 80% of absorption. These studies serve as a basis for design and realization of specific optimal geometries of meta-surface type with the 3D printing technique, in order to reach a high level of electromagnetic interference shielding performance for real world EM cloaking and EM ecology applications. © 2016 AIP Publishing LLC.

[<http://dx.doi.org/10.1063/1.4945576>]

## I. INTRODUCTION

Microwave is the ultimate range for open space communication. However, drastic growth of the satellite data transmission in the past decade makes the spectral bands allocated to the different communication channels overcrowded.<sup>1</sup> Along with the ever-increasing density of emitters in the environment, this crowd makes the electromagnetic (EM) compatibility an important issue. In other words, any new equipment must have adequate immunity in order to function consistently and reliably, be resilient to major disturbances, and coexist with other equipment. Thus, one needs new functional materials combining high electrical conductivity and good electromagnetic (EM) interference shielding effectiveness (SE)—the reciprocal of the transmission factor—for electromagnetic coatings, shields, and filters, working in specific frequency bands.

The electromagnetic interference (EMI) shielding effectiveness (SE) is determined by material absorptivity, surface reflectivity, and multiple internal reflections. For a continuous

metal sheet, the latter mechanism is negligible. In conventional macroscopic materials such as nonmagnetic metals, the absorption mainly takes place across the skin depth, which decreases with the frequency. The EMI SE can be written<sup>1</sup> as

$$SE = 20 \cdot \log_{10} \left( \sqrt{\frac{\sigma}{\pi f \epsilon_0}} \right) - 20 \cdot \log_{10} 4 + 20t \sqrt{\pi f \mu_0 \sigma} \log_{10} e,$$

where  $\sigma$  is the shielding material conductivity,  $f$  is the frequency of the incoming EM wave,  $t$  is the thickness of the shielding layer, and  $\mu_0$  and  $\epsilon_0$  are vacuum permeability and permittivity, respectively. Therefore, at frequencies above 5 GHz for a Cu foil, being 100  $\mu\text{m}$  thick with conductivity  $\sigma = 5.7 \times 10^7 \text{ S/m}$ , one expects to have the EMI SE at the level more than 30 dB caused by an almost 100% reflection. The problem is that the reflection is a source of a secondary EMI pollution. That is why the possibility to have as high EM attenuation as possible coming from the absorption losses is very attractive.

The EMI SE of a composite material mainly depends on the filler's intrinsic conductivity, dielectric constant, and aspect ratio.<sup>2</sup> Nano-carbon fillers, such as graphene nanoplatelets and carbon nanotubes, are indeed interesting materials

<sup>a)</sup>Author to whom correspondence should be addressed. Electronic mail: polina.kuzhir@gmail.com. Tel.: +375 17 200 7410.

<sup>b)</sup>URL: <http://3dkivansag.blog.hu/>

<sup>c)</sup>URL: <http://www.nanotechnology.hu/>

from the point of view of electromagnetic shielding. Although many studies of the electromagnetic properties of graphene based polymer composites are available, the graphene nanocomposites' research is still at a very early stage of evolution especially from the view point of EMI shielding material development.<sup>3–6</sup> Combination of strategies like multilayered structures and hybrid fillers are expected to provide an effective solution to realize a lightweight, mechanically strong, processable, and economically viable shielding material suitable for commercial and defense sectors.<sup>7</sup>

Recently, we demonstrated<sup>8,9</sup> that multilayered structures of alternating graphene monolayers and polymer layers can provide an efficient shield against microwave radiations achieving up to 50% absorption of the incident radiation energy at normal incidence. The magnitude of the absorption depends on the number of graphene sheets and the doping level. Though graphene/polymer heterostructures have several advantages in comparison with conventional metal shielding layers, such as lightweight, resistance to corrosion, and flexible absorption mechanism of shielding, their fabrication process is quite difficult because of graphene transfer stage. The very thin multilayer sandwiches are not easy to be produced and characterized due to the difficult sample handling. Such multilayered sandwich structures can protect micro- and nano-devices in a harsh electromagnetic environment, due to the promising electromagnetic shielding efficiency of graphene.<sup>9</sup> Many specific factors, e.g., thickness, microstructure, number of graphene layers, and texture, may have strong influence on the electromagnetic properties of sandwich graphene/polymer structures. However, stronger films and more reliable processing conditions are required to meet different application needs.

Ordered and disordered photonic crystal type structures,<sup>10</sup> composed of periodic dielectric or metal-dielectric nanostructures, provide an ultimate control of electromagnetic waves<sup>11–13</sup> in microwave-to-THz range. Various advanced processing and manufacturing techniques have been proposed for the fabrication of photonic crystal structures such as layers deposition, lithography, and direct laser writing. We have used the additive manufacturing (3D printing), which makes it possible to use different materials, with very different properties at geometrically precisely defined spatial positions. Therefore, it will be a very attractive way of constructing complex architectures from different materials, which would not be possible to be produced in a simple way by conventional technologies.

In this study, our idea was to design a new type of light material having tunable EM electromagnetic absorption properties by 3D printing of photonic type band gap structures by layer by layer deposition of nano-carbon doped polymer layers and pure (dielectric) polymer layers. The source material for the nano-carbon layer is a commercial nanocomposite filament, named 3D Black Magic (3DBM),<sup>14</sup> consisting of a nano-carbon filler incorporated in a polylactic acid (PLA) polymer, while the pure polymer layer is printed from a pure PLA filament. We study the electromagnetic wave propagation in those periodic nano-carbon/polymer structures and relate this with the texture, structure, and thermal properties. The applicability of the nano-carbon/polymer

sandwich materials for protection of micro and nano-electronic devices in microwave and THz range is discussed.

## II. EXPERIMENTAL

### A. Materials and manufacturing of 3D printed multilayered structures

For printing the sandwich structures, we used the commercial 3DBM filament, which is a composite of Polylactic acid (PLA) thermoplastic doped with highly conductive nano-carbon materials (according to supplier information, 10 wt. % of nano-carbon inclusions are added to the PLA). A commercial pure PLA filament was used to print the dielectric polymer layers, which separate the nano-carbon doped layers. The 3D printed multilayered structure was fabricated by layer by layer deposition of a 0.1 mm thick pure PLA layer, followed by a 0.1 mm Black Magic Layer (BML). The structural unit composed of a carbon doped PLA layer (called here nano-carbon layer, BML) and a pure PLA layer may be repeated several times. Multilayered samples containing from 1 to 4 nano-carbon layers were produced by using a Fused Filament Fabrication/Fused Deposition Modeling (FFF/FDM) 3D printer with dual head extruder (extruder temperature: 230 °C; table heating: 50 °C; speed: 30 mm/s; extrusion multiplier 1.1). Rectangular samples and disk shaped ones having thickness from 0.4 mm to 1.0 mm were printed for direct electromagnetic measurements. The following samples were printed: multilayer samples containing 1–4 nano-carbon layers separated by PLA layers (named BML1-PLA, BML2-PLA, BML3-PLA, and BML4-PLA), and reference samples (REF1–REF4) consisting the same number of layers as the corresponding PML<sub>x</sub>-PLA sample, but without nano-carbon content (all layers printed from the pure PLA filament).

### B. Structural characterization

Transmission electron microscope (TEM) analysis using JEOL JEM 2100 at accelerating voltage 200 kV was performed for characterization of the carbon nanostructures in the commercial filament. The homogeneity and the degree of dispersion of the nano-carbon dopant in the 3D printing filament were checked by Optical Microscopy (OM) in thin sections of 1 μm in thickness prepared by microtome sectioning after incorporation in a special resin. Samples for Cross Section Transmission Electron Microscopy (X-TEM) (Philips CM20) were prepared by ultramicrotome sectioning to a thickness of 70 nm.

### C. Electromagnetic characterization

Measurements of dielectric characteristics of 3D Black Magic filament for 3D printer as they are in low frequency range from 20 Hz to 2 MHz were done using LCR meters HP4284A.

The microwave measurements were provided by a scalar network analyzer R2-408R (ELMIKA, Vilnius, Lithuania) at room temperature and normal pressure. The system consists of a sweep generator, waveguide reflectometer, network analyzer, and indicator unit (personal computer). The scalar

network analyzer is designed for measurement of the transmission factor (attenuation) and reflection factor module Voltage Standing Wave Ratio (VSWR) of waveguide devices and components in frequency range from 25.96 GHz to 37.5 GHz. The frequency sweep bandwidth range can vary from the full frequency range of the instrument to 1500 MHz. The set-up provides automatic frequency sweep over the full frequency range with a sweep time of  $0.08 \pm 0.016$  s or  $1.0 \pm 0.2$  s. Basic error limit of the frequency setting does not exceed  $\pm 0.2\%$  in normal conditions. In the panoramic measurement mode, the generator is operating in periodic frequency sweep from the start frequency to the end frequency of the sweep range. The output signal is modulated by 100 kHz square pulse modulation. Measurements are based on separation, by the directional couplers, of signals proportional to that incident to device under test (DUT) and that reflected from DUT mm-wave powers (in case of VSWR measurements) or proportional to incident and passed through DUT (in case of attenuation measurements) mm-waves. The IEC 62431:2008(E) standard specifying the measurement method for the reflectivity of EM materials for the normal incident is used. The EM response of the samples as ratios of transmitted/input ( $S_{21}$ ) and reflected/input ( $S_{11}$ ) signals has been measured in the 26–37 GHz frequency range (K<sub>a</sub>-band). The frequency stability of the oscillator was controlled by a frequency meter and was as high as  $10^{-6}$ . The power stabilization was maintained in the level of  $7.0 \text{ mW} \pm 10 \mu\text{W}$ . EM attenuation was measured in the 0 dB to  $-40$  dB range. Basic measurement errors of EM attenuation over the range 0–25 dB were  $\delta|S_{21}| = \pm(0.6 + 0.06|S_{21}|)$ . After a standard procedure of instrument calibration for transmission and reflection measurements, the  $S$ -parameters were measured by subsequent insertion of the samples into the waveguide. The accuracy has been controlled by repetitive measurements. Reflectance ( $R$ ), transmittance ( $T$ ), and absorbance ( $A$ ) values are obtained from the measured  $S$ -parameters in the following way:  $R = S_{11}^2$ ,  $T = S_{21}^2$ , and  $A = 1 - R - T$ . The scheme of the waveguide measurements is presented in Fig. 1(a).

THz measurements were carried out using a commercial THz time-domain spectrometer (T-SPEC Ekspla, Vilnius, Lithuania).  $1050 \pm 40$  nm wavelength pumping laser having 50–150 fs pulse duration and more than 40 mW output power at approximately 80 MHz pulse repetition rate was used to excite a photoconductor antenna and produced THz radiation up to 2 THz. The layout of the system is shown in Fig. 1(b). The spectrometer THz emitter and detector consist of a micro strip antenna integrated with photoconductor (low temperature grown GaBiAs) and silicon lens. THz detector output is proportional to the instant electrical field strength of THz pulse during ultrashort pumping pulse. The Fourier transform of waveform of electrical field of THz radiation gives the spectral content ( $E(\omega)$ ) of THz radiation. A comparison of the spectra with ( $E_{\text{sample}}(\omega)$ ) and without ( $E_{\text{ref}}(\omega)$ ) sample inserted into THz beam under normal incidence gives the complex transmission function ( $t(\omega) = E_{\text{sample}}(\omega)/E_{\text{ref}}(\omega)$ ) of the sample under investigation. To get better signal to noise ratio, 1024 scanned curves averaging was used.

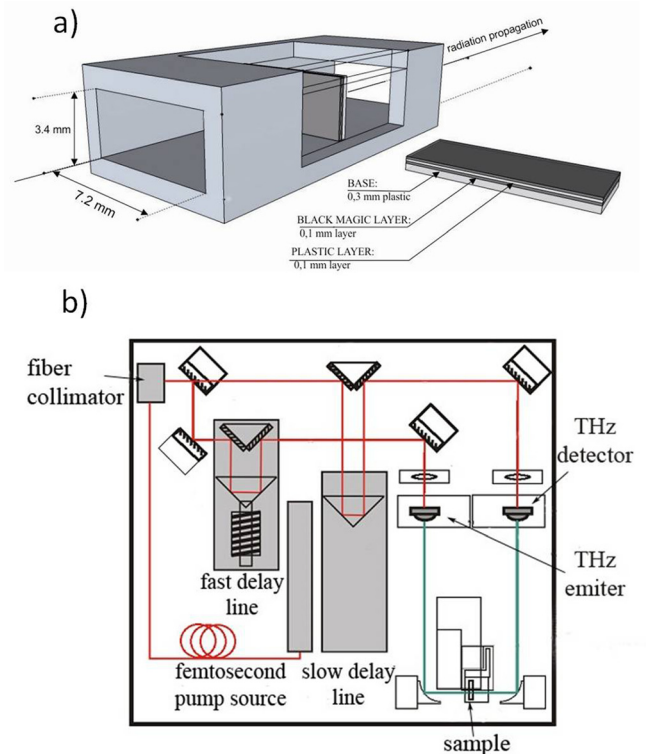


FIG. 1. (a) The waveguide measurement setup. Electromagnetic wave propagates along the  $z$  axis. (b) Scheme of the terahertz time-domain spectroscopy setup (T-SPEC Ekspla).

#### D. Thermal characterization

Differential Scanning Calorimetry (DSC) was performed using a DSC Q20 TA Instruments with two heating cycles from  $30^\circ$  to  $200^\circ\text{C}$  at  $10^\circ\text{C}/\text{min}$  separated by a single cooling cycle at  $10^\circ\text{C}/\text{min}$  with isothermal steps for 5 min at  $200^\circ\text{C}$  and 2 min at  $30^\circ\text{C}$ . The amount of samples for the DSC analysis was 4–5 mg. For reference sample, an empty pan was used. The DSC curve from the first run of the experiment was used to determine the glass transition temperature ( $T_g$ ), crystallization temperature ( $T_c$ ), crystallized fraction ( $\chi\%$ ), and melting temperature ( $T_m$ ).

Thermogravimetric analysis (TGA) was carried out using a TG Q50 Analyzer (TA Instruments). The samples were heated within the temperature range  $30$ – $550^\circ\text{C}$  with a heating rate of  $10^\circ\text{C}$  per minute in air atmosphere. The thermal stability at 10% mass loss ( $T_{10\%}$ ), thermal degradation ( $T_p$ ), and final weight loss (%) are the characteristics taken from the TGA curve.

### III. RESULTS

#### A. Structural characterization of the nano-carbon filament

Figures 2(a) and 2(b) show the optical microscopy images in transmitted light through the  $1 \mu\text{m}$  thick cross section of the 3D Black Magic (3DBM) filament. Prior to microtome sectioning, the filament was incorporated in special resin. The images in two magnifications (scale bars of  $200 \mu\text{m}$  (a) and  $20 \mu\text{m}$  (b)) demonstrate the homogeneity of

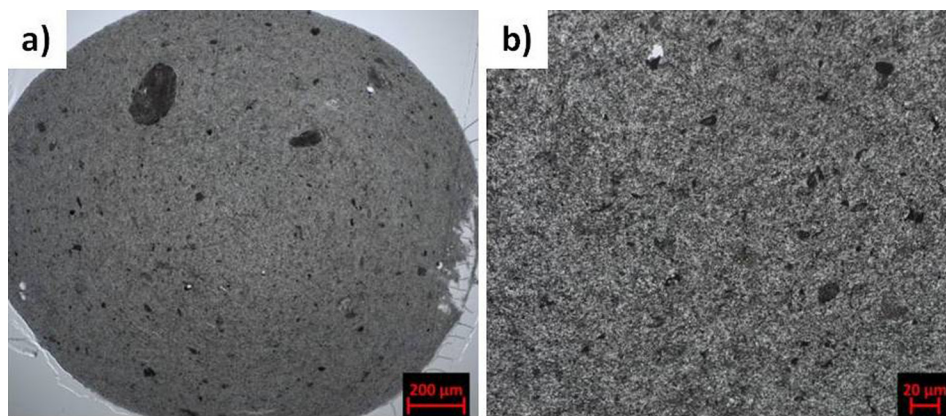


FIG. 2. Cross sectional optical microscopy images in transmitted light through sections of  $1\ \mu\text{m}$  thickness of the 3DBM filament. Prior to microtome sectioning, the filament was incorporated in special resin.

dispersion of the nano-carbon dopant in the 3D printing filament. As can be seen, the nano-carbon filler does not present segregation, only a few large agglomerates of  $100\text{--}200\ \mu\text{m}$  size are visible as black spots.

In Fig. 3(b) at higher magnifications, it is seen that the nano-carbon dopant is uniformly distributed in the polymer matrix. The nano-carbon filler is obviously a mixture of milled short carbon nanotubes and other structures.

In order to characterize the type of nano-carbon structures used as a dopant of PLA inside the Black Magic filament, the thin films were heated to  $500\ ^\circ\text{C}$  at a heating rate of  $10\ ^\circ\text{C}/\text{min}$  using thermogravimetric analysis. At these TGA heating conditions, the polymer is burned, but the nano-carbon filler is not degraded and remains in the residue char. Transmission electron microscopy analysis was performed for the residue char for further visualization. For the TEM study, a preliminary preparation technique was applied. The residue char was dispersed in ethanol, and a micro-quantity of colloid was dropped on standard copper TEM grid covered by amorphous carbon membrane then dried in dust-free atmosphere at ambient conditions. The phase composition of the colloids was determined by selected area electron diffraction (SAED) mode of the microscope. Figs. 4(a)–4(c) present the TEM micrographs at different locations of the carbon ash residue. As can be seen, the Black magic filament contains a mixture of carbon nanostructures, mostly graphene sheets (a), short multiwall carbon nanotubes (b), and carbon cone-like structures (c).

## B. Structural characterization of the 3D printed multilayer sandwiches

Figure 5(a) shows the optical image of the cross section of an example 3D printed sandwich type sample (BML4-PLA), where the multilayer structure consists of a base PLA layer ( $0.3\ \text{mm}$  thick), 4 nano-carbon layers ( $0.1\ \text{mm}$  black stabs), separated by pure PLA layers ( $0.1\ \text{mm}$  grey stabs). The sandwich structure is made from continuous alternating layers. Fig. 5(b) presents the X-TEM micrograph of the PLA/nano-carbon doped interface in the multilayered sandwiches. The interface is sharp and continuous; the nano-carbon additive has kept its good dispersion and homogeneity during the 3D printing process (Fig. 3(b)).

## C. Thermal properties

The thermal properties of the 3D printed multilayered sandwiches with 1 and 4 nano-carbon layers (samples BML1-PLA and BML4-PLA) were investigated by differential scanning calorimetry and thermogravimetric analysis, as well as compared to the reference pure PLA samples (REF) having the same number of layers.

The results from DSC analysis are presented in Fig. 6, where the thermograms plot the heat flow vs. temperature. The glass transition ( $T_g$ ), the crystallization ( $T_c$ ), and melting ( $T_m$ ) temperatures are determined from the peaks of the DSC curves (1st run) and shown in Fig. 6. Table I summarizes the calorimetrical characteristics of the three sample materials. Our results show that the nano-carbon doped PLA, fabricated

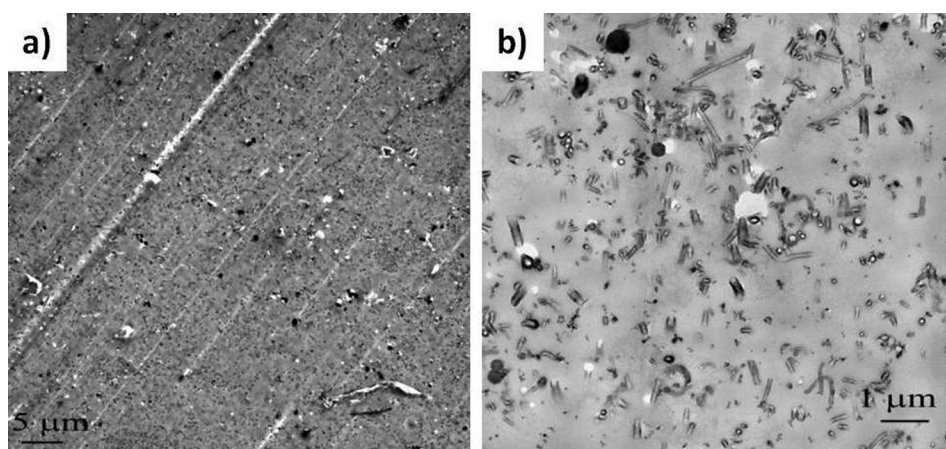


FIG. 3. X-TEM of the 3DBM filament at two magnifications. (a) The diagonal lighter lines are artefacts generated by the imperfections of the diamond knife of the ultramicrotome and (b) the nano-carbon dopant is uniformly distributed in the polymer matrix.

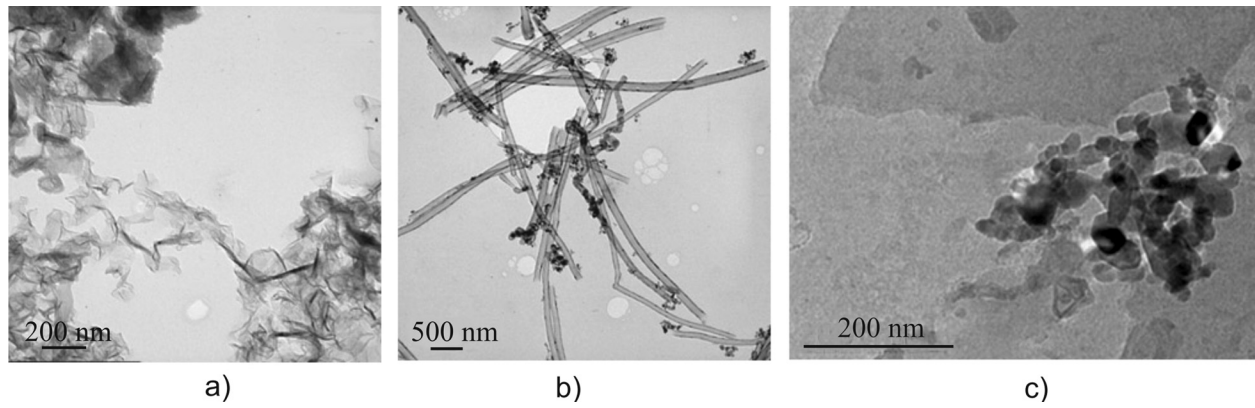


FIG. 4. TEM micrographs of the residue char after burning of filament at 500 °C. Three different nano-carbon structures were identified in the Black Magic filament: (a) graphene; (b) multiwall carbon nanotubes; and (c) carbon cone-like structures.

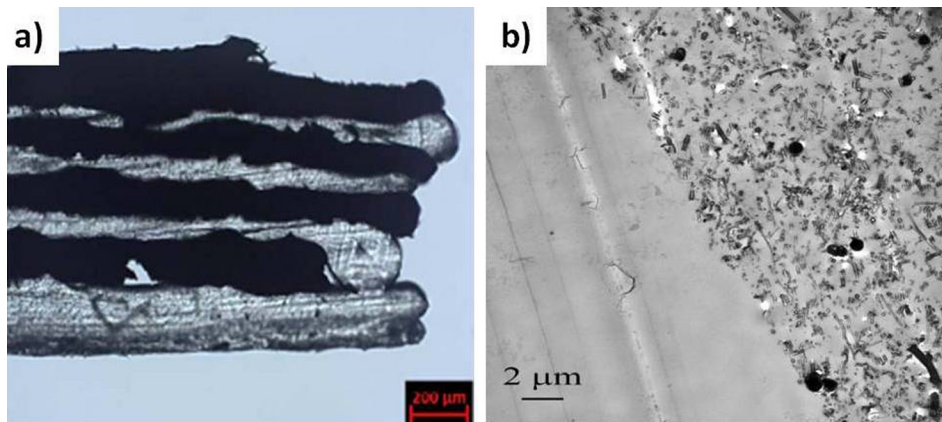


FIG. 5. (a) Optical image of the cross section of 3D printed multilayered sample with 4 nano-carbon layers (black stabs) and (b) X-TEM image of the PLA/nano-carbon doped interface.

via melt blending, has negligible impact on  $T_g$ . In general, the effects of the graphene nanofiller on glass transition temperature ( $T_g$ ) remain controversial. Some authors reported that composites with small amount of several types of nanofillers indicate a negligible impact on  $T_g$ .<sup>15</sup> Liao *et al.*<sup>16</sup> found no changes in  $T_g$  for graphene/polymer nanocomposites synthesized via physical blending processes such as

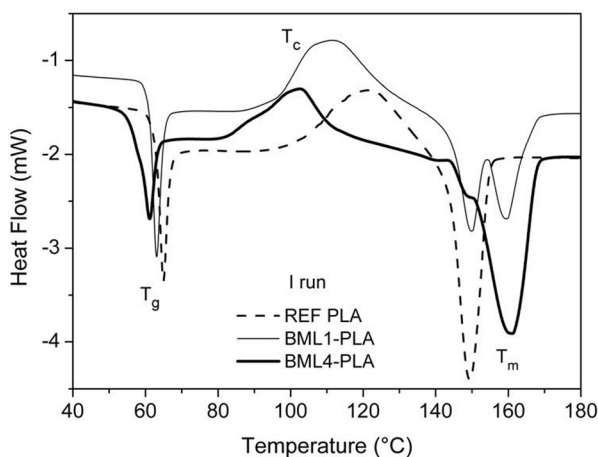


FIG. 6. DSC thermograms of heat flow vs. temperature for the 3D printed sandwich structures with one and four nano-carbon layers (BML1-PLA and BML4-PLA), compared to the reference pure PLA sample (REF). The glass transition ( $T_g$ ), crystallization peak ( $T_c$ ), and melting peak ( $T_m$ ) temperatures are shown.

solvent or melt blending, except for blending with strongly polar polymers, while, chemical blending processes such as *in situ* polymerization or chemically modified graphene yielded significant increases in  $T_g$  for nanocomposites.

Importantly, we found that the  $T_c$  temperatures for the nano-carbon containing sandwich structures are strongly shifted towards lower temperatures with increasing the number of nano-carbon layers from 1 to 4. The crystallized fraction ( $\chi\%$ ) gradually decreases from 23.9% for the pure PLA to 22.0% for one nano-carbon layer and to 10.2% for the 4 nano-carbon layers sandwiches. This confirms that graphene exhibits nucleation effect,<sup>17</sup> which leads to a decrease of the nucleus size by increasing the nano-carbon filler content in the sandwich structures. Double melting peak ( $T_m$ ) was observed for the nano-carbon containing sandwich samples, which is associated with the presence of two materials. The second melting temperature is about 10 °C higher than the first melting temperature. Thus, we assume that the first  $T_m$  peak represents the melting temperature of the pure PLA polymer, while the second melting peak may be associated with the melting temperature of the nano-carbon doped PLA composite material.

Thermal stability is an important property for polymer nanocomposites. The TG and Derivative Thermogravimetric Analysis (DTG) curves for the pure PLA and BML-PLA sandwich structures with one and four layers are illustrated in Fig. 7. The characteristic temperatures are tabulated in

TABLE I. Thermal characteristics of the nano-carbon containing sandwich structures and the reference PLA at temperature range 30–550 °C and heating rate 10 °C/min in air atmosphere.

Sample	$T_g$ (°C)	$T_c$ (°C)	$T_m$ (°C)	Crystallized fraction ( $\chi\%$ )	$T_{10\%}$ (°C)	$T_p$ (°C)	Char (%)
REF PLA	64.2	122.2	149.4	23.9	328.6	364.6	0.004
BML1-PLA	62.2	111.0	149.7 159.9 <sup>a</sup>	22.0	319.2	360.0	1.73
BML4-PLA	60.3	102.4	148.1 161.3 <sup>a</sup>	10.2	321.6	359.8	4.17

<sup>a</sup>Double melting peak ( $T_m$ ).

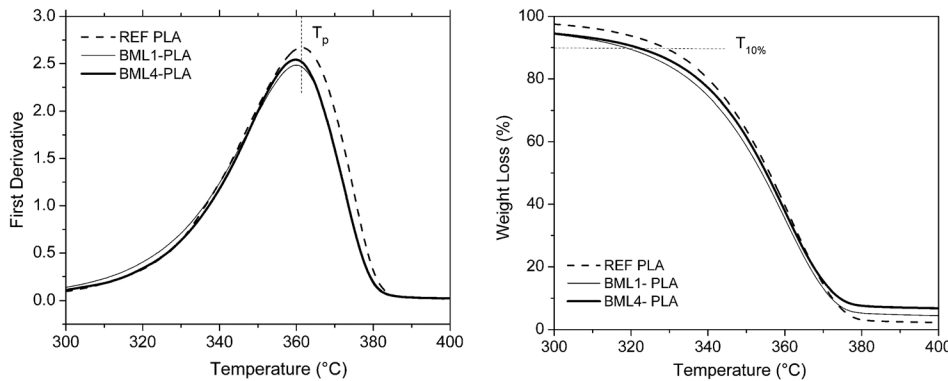


FIG. 7. (a) TGA thermograms and DTG curves (b) of the multilayered sandwiches with 2 and 4 nano-carbon layers compared to the reference PLA sample in the temperature range 30–550 °C at heating rate 10 °C/min in air atmosphere.

Table I for comparison purposes. The thermal behavior of PLA and its nanocomposites shows a single degradation stage. The nano-carbon doped PLA sandwiches have slightly lower thermal stability ( $T_{10\%}$ ) than pristine PLA. The decrease of the PLA thermal stability may be associated with the presence of nano-carbon filler as plasticizer in the Black Magic filament by its action to intersperse itself around polymers and by breaking polymer-polymer interaction, which are predicted in the lubricity theory and the gel theory of plasticization.<sup>18,19</sup> The degradation temperature ( $T_p$ ) peak at which the decomposition appears is similar for the three samples. The final weight loss (residue char) at 500 °C is of 1.73 and 4.17 wt. %, for BML1-PLA and BML4-PLA samples, respectively. The residue char represents the amount of the non-degraded nano-carbon filler in both studied sandwich samples. The residue char quantity for the reference PLA sample is very small  $\sim 0.004\%$ , which demonstrates the full degradation of the PLA polymer.

In general, the temperature dependent structural characteristics, such as glass transition, crystallization, and melting, are strongly affected by the presence and the number of nano-carbon layers in the sandwich structure. However, the effects of nano-carbon layers on the thermal stability and degradation of multilayered materials are insufficient.

#### D. Microwave properties

Electrical conductivity and dielectric permittivity of Black Magic filament for 3D printer in a wide frequency range from static regime to 2 MHz were collected in Table II. According to these data, i.e., ac conductivity in all frequency range is not less than 54 S/m and dielectric permittivity is from  $4 \times 10^6$  at 20 Hz to  $10^4$  at 2 MHz, the Black Magic filament content is well above the percolation threshold.

No significant frequency dependence of the EM response properties was observed in Ka-band (26–37 GHz), therefore, all results are presented at frequency 30 GHz. One can see from Fig. 8(a) that the base plastic is transparent for microwave radiation, whereas adding only one nano-carbon doped layer of Black Magic filament leads to a decrease of transmittance to less than 20%.

The main contribution to EM attenuation of the one-nano-carbon layer sandwich structure (BML1-PLA) comes from reflection (approx. 55%), but absorption is also significant (almost 30%). This EMI SE is really good for so thin polymer composite layer as 100  $\mu\text{m}$ . It is compatible with what was observed for 1 mm thick epoxy filled with carbon nanotubes, carbon black, graphene platelets, or carbon onions.<sup>20</sup> Two, three, and four BMLs make the sandwich structure opaque for GHz signals due to more than 60% of reflection and 30%–40% absorption. Note that the reflection reaches its maximum at 2 nano-carbon-containing layers, whereas the absorption remains increasing. Finally, as summarized in Fig. 8(a), EMI SE or  $-S_{21}$  is as high as 8, 11, 12, and 15 dB for 1–4 nano-carbon doped layers.

#### E. Terahertz properties

The squared absolute values of the complex transmission function (transmittance) for reference samples and samples contacting 1–3 nano-carbon layers are presented in

TABLE II. Electrical conductivity and dielectric permittivity of Black Magic filament for 3D printer in frequency range from 20 Hz to 2 MHz.

Frequency	20 Hz	100 Hz	1 kHz	2 MHz
Real part of dielectric permittivity	$4 \times 10^6$	$7 \times 10^5$	$9 \times 10^4$	$10^4$
Electrical conductivity (S/m)	54.8	54.9	55.0	55.2

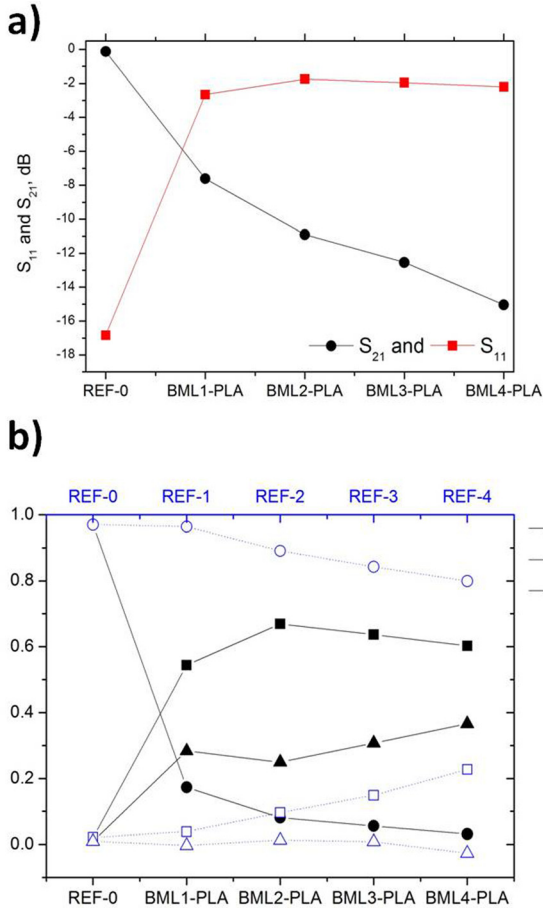


FIG. 8. (a) Measured S-parameters of nano-carbon containing sandwich structures in dB at 30 GHz. (b) Reflectance, absorbance, and transmittance reconstructed from the experimental data of reference samples (open symbols) and samples contacting 1–4 nano-carbon layers (solid symbols) at 30 GHz.

Fig. 9. The background level (see Fig. 9(a)) clearly shows that transmittance through BML1 and BML2 are significantly above the device accuracy limit in spite the level of transmission is very low,  $\leq 10^{-2}$  and  $\leq 10^{-3}$  for BML1 and BML, respectively. As compared to microwave response, in THz frequency range, the transmittance of the base plastic is around 50% and decreases with the frequency. Addition of only one nano-carbon layer strongly reduces the transmittance level, and the sample consisting of 1–3 BML becomes opaque for electromagnetic radiation in THz frequency range.

In order to describe the measured results, we utilized the following model. The real and imaginary parts of the complex transmission function  $t(\omega)$  can be calculated from the solution of the boundary problem for the multi-layer system. Let us consider the double-layer system comprising a base plastic and one nano-carbon layer (BML1-PLA sample). Using the continuity condition of tangential components of the electric and magnetic field on the vacuum/base plastic layer-, base plastic layer/nano-carbon layer-, and nano-carbon layer/vacuum interfaces (see inset in Fig. 9(b)), the following system of equations can be written:

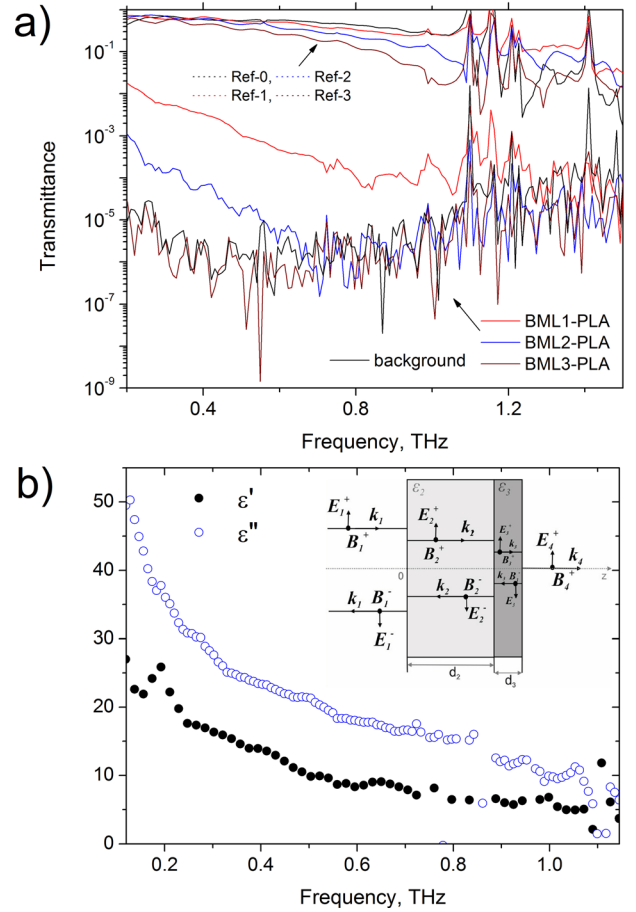


FIG. 9. (a) Terahertz transmittance spectra of reference samples and samples contacting 1–3 nano-carbon layers. (b) Frequency dependence of the real and imaginary parts of the complex dielectric permittivity for BML1-PLA. In the numerical calculation, we used the complex dielectric permittivity value  $\epsilon = 2.9 + 0.29i$  for the base plastic, which was calculated from the experimental data obtained for the REC-0 sample. The thickness of nano-carbon and plastic layers was set 0.1 and 0.3 mm, respectively.

$$\begin{aligned}
 (E_1^+ - E_1^-) - (E_2^+ - E_2^-) &= 0 \\
 \sqrt{\epsilon_2}(E_2^+ + E_2^-) - (E_1^+ + E_1^-) &= 0 \\
 (E_2^+ \exp(id_2k_2) - E_2^- \exp(-id_2k_2)) - (E_3^+ \exp(id_2k_3) \\
 - E_3^- \exp(-id_2k_3)) &= 0 \\
 \sqrt{\epsilon_3}(E_3^+ \exp(id_2k_3) + E_3^- \exp(-id_2k_3)) \\
 - \sqrt{\epsilon_2}(E_2^+ \exp(id_2k_2) + E_2^- \exp(-id_2k_2)) &= 0 \\
 (E_3^+ \exp(i(d_2 + d_3)k_3) - E_3^- \exp(-i(d_2 + d_3)k_3)) \\
 - E_4^+ \exp(i(d_2 + d_3)k_4) &= 0 \\
 E_4^+ \exp(i(d_2 + d_3)k_4) - \sqrt{\epsilon_3}(E_3^+ \exp(i(d_2 + d_3)k_3) \\
 + E_3^- \exp(-i(d_2 + d_3)k_3)) &= 0, \quad (1)
 \end{aligned}$$

where  $k_i$ ,  $\epsilon_i$ , and  $d_i$  are the wavenumbers, dielectric permittivity, and thickness values of the  $i$ th medium, respectively. The coefficients  $E_i^\pm$  are the complex amplitudes of the electric field in  $i$ th medium. The “+” and “-” superscripts signify the forward and backward propagating waves (see inset in Fig. 9(b)). Solving the system (1) of 6 equations for  $E_1^-$ ,  $E_2^\pm$ ,  $E_3^\pm$ ,  $E_4^+$ , one comes to expression (2) for the complex transmission function  $t(\omega)$  of BML1 and PLA

$$t(\omega) = \frac{E_4^+}{E_1^+}, \quad (2)$$

which already does not depend on the amplitude of the incident wave, but on the constitutive electromagnetic parameters (permittivity) of both BML and PLA layers.

Thus, for the sample containing only one nano-carbon layer being 0.1 mm thick on a 0.3 mm thick plastic substrate, the comparison of experimental data with the above described model allows us to estimate the dielectric permittivity of the nano-carbon material in THz frequency range (Fig. 9(b)).

As it can be seen from Fig. 9(b), the absolute value of the imaginary part ( $\epsilon''$ ) of the complex permittivity is larger than that of the real part ( $\epsilon'$ ) and both of them decrease with frequency. Such frequency behavior is specific to polymer composites with different carbon inclusions (for Carbon nanotubes, carbon onions, graphene nanoplatelets, and carbon black) above the percolation threshold<sup>21–27</sup> and can be explained by influence of a Drude term on the total conductivity of inclusions in this frequency area.<sup>28,29</sup>

The frequency dependence of absorption, reflection, and transmission coefficient of BML1-PLA samples when the radiation goes through the base substrate first (b) and opposite case (a) are presented in Fig. 10. For these samples,

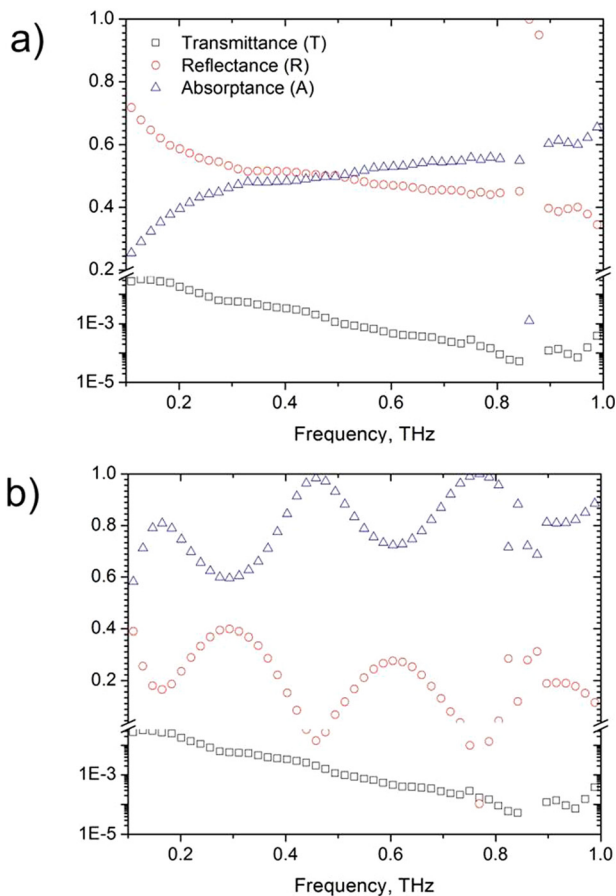


FIG. 10. Frequency dependence of absorption, reflection, and transmission coefficient of BML1-PLA sample: (a) the incident EM waves come from the side of the nano-carbon layer and (b) the incident EM waves come from the side of the PLA layer.

where there is a significant difference between permittivity of the base layer and carbon containing layer (2.8 vs 15 for real part), it is important from which side the radiation arrives at the sample. When the incoming radiation comes from the side of the base layer then 20% of reflection comes from the base layer itself, the rest is absorbed in the carbon containing layer after multiple reflections within this layer. The observed peaks in the reflectance spectra (see Fig. 10(b)) are due to interference effects on the base layer thickness. The high level of reflection on the border between base and BML layers as well as high absorption in BML layer leads to a small level of transmission through such a system and a resultant transmission spectrum does not show interference picture.

When the incoming radiation comes from the side of the BML layer, however, approximately 50% is reflected from the more “metallic” carbon layer, and then the rest is absorbed in the base- and carbon-containing layers. Thus, in the sense of absorption, the incoming direction base-sandwich is preferable.

#### IV. CONCLUSIONS

The results demonstrate the unlimited potential of the 3D printing technique for producing multilayered structures by layer by layer deposition. The sandwich structure composed of continuous nano-carbon doped polymer layers and pristine polymer layers, the mixed nano-carbon filler consisting of graphene, short carbon nanotubes, and carbon cone-like structures obviously determines both the microwave and the thermal properties of the complex material.

The temperature dependent structural characteristics, crystallization, and melting are strongly affected by the presence and the number of nano-carbon doped layers in the sandwich structure. The crystallization temperature ( $T_c$ ) and the crystal fraction of the sandwich structures strongly decrease with an increasing number of nano-carbon layers, confirming the nucleation effect of graphene on PLA. Double melting peak ( $T_m$ ) was observed, which is associated with the presence of two materials in the sandwich structure, the pristine PLA layer, and the layer of nano-carbon doped PLA. However, nano-carbon doped PLA fabricated via melt blending has negligible effect on  $T_g$ , as well as insufficient impact on the thermal stability and degradation of the multilayered sandwich materials.

The electromagnetic measurements promise a great potential of such a type of materials for electromagnetic compatibility applications in microwave frequency range. Sandwich structures containing only two nano-carbon layers already become nontransparent to the microwaves, giving EMI SE at the level of 8–15 dB, and the contribution of absorption of the plane stratified sandwich structure is quite significant (30%–40%). In case of upgrading the structure with proper anti-reflection geometry, we may obtain the same zero transmission originated from the full absorption (see, e.g., Ref. 30).

The level of both the real ( $\epsilon'$ ) and imaginary parts ( $\epsilon''$ ) of permittivity of the produced 3D printed sandwich structures in THz range is as high as 30–10 and 50–10, respectively,

and it decreases with the frequency. In the case when the base (plastic) substrate meets the THz radiation first, 20% of the reflection comes from the very first (base) layer, and the rest, 80%, absorbed in BML after multi-reflection within the carbon containing layer. The next step could be a design and realization of specific optimal geometries of meta-surface type with 3D printing technique in order to provide a high level of electromagnetic interference shielding performance for utilization of nano-carbon containing sandwich structures for real EM cloaking and EM ecology applications.

## ACKNOWLEDGMENTS

This work was carried out within the framework of the FP7-FET Flagship 604391 Graphene and IRSES-2012-318617 FAEMCAR, U.S. Air Force through CRDF Global Agreement Grant No. AF20-15-61804-1, P.K. and S.M. are thankful for the support by Tomsk State University Competitiveness Improvement Program, A.P. acknowledges FP7 project FP7-316633 POCAONTAS. The authors are thankful to Professor Philippe Lambin for valuable discussions. We are thankful to Dr. Vitali Ksenevich, Belarusian State University, for having performed low frequency measurements of Black Magic 3D filament.

<sup>1</sup>H. Ott, *Electromagnetic Compatibility Engineering* (John Wiley & Sons, New York, 2009).

<sup>2</sup>M. B. Bryning, M. F. Islam, J. M. Kikkawa, and A. G. Yod, *Adv. Mater.* **17**, 1186 (2005).

<sup>3</sup>S. Stankovich, D. A. Dikin, G. H. Dommett, K. M. Kohlhaas, E. J. Zimney, E. A. Stach, R. D. Piner, S. T. Nguyen, and R. S. Ruoff, *Nature* **442**, 282 (2006).

<sup>4</sup>V. Eswaraiyah, V. Sankaranarayanan, and S. Ramaprabhu, *Macromol. Mater. Eng.* **296**, 894 (2011).

<sup>5</sup>H. B. Zhang, Q. Yan, W. G. Zheng, Z. He, and Z. Z. Yu, *ACS Appl. Mater. Interfaces* **3**(3), 918–924 (2011).

<sup>6</sup>J. Liang, Y. Wang, Y. Huang, Y. Ma, Z. Liu, J. Cai, C. Zhang, H. Gao, and Y. Chen, *Carbon* **47**(3), 922–925 (2009).

<sup>7</sup>P. Saini and M. Arora, in *New Polymers for Special Applications*, edited by A. De Souza Gomes (Intech, 2012), Chap. 3.

<sup>8</sup>K. Batrakov, P. Kuzhir, S. Maksimenko, A. Paddubskaya, S. Voronovich, Ph. Lambin, T. Kaplas, and Yu. Svirko, *Sci. Rep.* **4**, 7191 (2014).

<sup>9</sup>K. Batrakov, P. Kuzhir, S. Maksimenko, N. Volynets, S. Voronovich, A. Paddubskaya, G. Valusis, T. Kaplas, Yu. Svirko, and Ph. Lambin, “Enhanced microwave-to-terahertz absorption in graphene,” *Appl. Phys. Lett.* **108**, 123101 (2016).

<sup>10</sup>G. I. Márk, Z. Vértesy, K. Kertész, Z. Bálint, and L. P. Biró, *Phys. Rev. B* **80**, 051903 (2009).

<sup>11</sup>E. Yablonovitch, *Phys. Rev. Lett.* **58**, 2059 (1987).

<sup>12</sup>E. Yablonovitch, *J. Opt. Soc. Am. B* **10**, 283 (1993).

<sup>13</sup>C. K. Tsang, Z. Xu, and Y. Y. Li, *J. Electrochem. Soc.* **156**(11), D508–D512 (2009).

<sup>14</sup>See <http://www.blackmagic3d.com/Conductive-Graphene-3D-Printing-PLA-Filament-p/grphn-175.htm> for 3D Black Magic Filament.

<sup>15</sup>T. Ramanathan, A. A. Abdala, S. Stankovich, D. A. Dikin, M. Herrera-Alonso, R. D. Piner, D. H. Adamson, H. C. Schniepp, X. Chen, R. S. Ruoff, S. T. Nguyen, I. A. Aksay, R. K. Prud’Homme, and L. C. Brinson, *Nat. Nanotechnol.* **3**(6), 327–331 (2008).

<sup>16</sup>K. H. Liao, Sh. Aoyama, A. A. Abdala, and Ch. Macosko, *Macromolecules* **47**, 23 (2014).

<sup>17</sup>R. Valapa, S. Hussain, P. K. Iyer, G. Pugazhenth, and V. Katiyar, *J. Polym. Res.* **22**, 175 (2015).

<sup>18</sup>P. H. Daniels, *J. Vinyl Addit. Technol.* **15**, 219 (2009).

<sup>19</sup>B. W. Chieng, N. A. Ibrahim, W. Yunus, M. Z. Hussein, Y. Y. Then, and Y. Y. Loo, *Polymers* **6**, 2232 (2014).

<sup>20</sup>F. Qin and C. Brosseau, *J. Appl. Phys.* **111**, 061301 (2012).

<sup>21</sup>T. I. Jeon, K. J. Kim, C. Kang, I. H. Maeng, J. H. Son, K. H. An, J. Y. Lee, and Y. H. Lee, *J. Appl. Phys.* **95**(10), 5736–5740 (2004).

<sup>22</sup>Ch. Kang, I. H. Maeng, S. J. Oh, J.-H. Son, T.-I. Jeon, K. H. An, S. C. Lim, and Y. H. Lee, *Appl. Phys. Lett.* **87**(4), 041908 (2005).

<sup>23</sup>P. Kuzhir, A. G. Paddubskaya, S. A. Maksimenko, V. L. Kuznetsov, S. Moseenkov, A. I. Romanenko, O. A. Shenderova, J. Macutkevici, G. Valusis, and P. Lambin, *IEEE Trans. Electromagn. Compat.* **54**, 6 (2012).

<sup>24</sup>D. Bychanok, P. Kuzhir, S. Maksimenko, S. Bellucci, and C. Brosseau, *J. Appl. Phys.* **113**, 124103 (2013).

<sup>25</sup>D. S. Bychanok, A. G. Paddubskaya, P. P. Kuzhir, S. A. Maksimenko, C. Brosseau, J. Macutkevici, and S. Bellucci, *Appl. Phys. Lett.* **103**, 243104 (2013).

<sup>26</sup>P. Kuzhir, A. Paddubskaya, A. Plyushch, N. Volynets, S. Maksimenko, J. Macutkevici, I. Kranauskaite *et al.*, *J. Appl. Phys.* **114**, 164304 (2013).

<sup>27</sup>S. Bellucci, S. Bistarelli, A. Cataldo, F. Micciulla, I. Kranauskaite, J. Macutkevici *et al.*, *IEEE Trans. Microwave Theory Tech.* **63**, 2024 (2015).

<sup>28</sup>A. Ugawa, A. G. Rinzler, and D. B. Tanner, *Phys. Rev. B* **60**, R11305(R) (1999).

<sup>29</sup>J. Macutkevici, D. Seliuta, G. Valusis, R. Adomavicius, P. Kuzhir, A. Paddubskaya *et al.*, *Chem. Phys.* **404**, 129 (2012).

<sup>30</sup>D. Bychanok, S. Li, A. Sanchez-Sanchez, G. Gorokhov, P. Kuzhir, F. Y. Ogrin, A. Pasc, T. Ballweg, K. Mandel, A. Szczurek, V. Fierro, and A. Celzard, *Appl. Phys. Lett.* **108**, 013701 (2016).